

# Experimental Study on Three-Dimensional Bubble Rising Behaviours by Virtual Stereo Vision

Q. Feng, Q. Wang<sup>†</sup> and C.Y. Zhao

*School of Mechanical Engineering, Shanghai Jiao Tong University, 200240, Shanghai, China*

<sup>†</sup>Corresponding Author Email: [qianwang@sjtu.edu.cn](mailto:qianwang@sjtu.edu.cn)

(Received September 1, 2022; accepted December 1, 2022)

## ABSTRACT

This study addresses the measurement of three-dimensional (3D) bubble rising behaviour in still water with bubble equivalent diameters ranging from 2.61 mm to 5.11 mm using high-speed imaging and virtual stereo vision technology. The bubble shape, 3D trajectory/velocity, displacement angular frequency and terminal velocity of bubbles are analysed. The bubble equivalent diameter is obtained by the elliptic volume method. The bubbles are divided into small and large bubbles with a critical equivalent diameter of 4.49 mm, according to whether they are accompanied by deformation. The small bubbles ( $d_{eq} < 4.49$  mm) are spherical or ellipsoid, while the large bubbles ( $d_{eq} \geq 4.49$  mm) exhibit ellipsoid, mushroom and hat shapes. The 3D trajectory is obtained by 3D reconstruction of bubble centroid coordinates. The rising trajectory of small bubbles shows 3D spiral motion, while the pitch increases gradually with the increase in the equivalent diameter. The trajectory of large bubbles is a two-dimensional (2D) zigzag. The bubble displacement curves in  $x$ - and  $z$ -directions are evaluated with third-order Fourier fitting. The results show that the bubble displacement frequency in the  $x$ - and  $z$ -directions decreases with the increasing bubble diameter, and the displacement frequency in the  $x$ -direction is larger than that in the  $z$ -direction. The relative proportions of the viscous force, buoyancy, surface tension and inertial force on bubbles with different equivalent diameters are different, which leads to three trends in the vertical velocity of bubbles within the diameter range of this study. Finally, the bubble terminal velocity in still water is investigated. The terminal velocity first decreases and then increases with the increase in the equivalent diameter. The minimum value is 16.17 cm/s when the diameter of the bubble equivalent diameter is 4.49 mm. Moreover, the applicability of some classical prediction models is discussed.

**Keywords:** Bubble behaviour; Three-dimensional reconstruction; Deformation; Terminal velocity.

## NOMENCLATURE

$a$	ellipsoid major axis	$Sr$	Strouhal number, $Sr = \frac{fd_{eq}}{V_T}$
$b$	ellipsoid minor axis	$T$	camera shift vector
$c$	polar diameter	$T_h$	threshold
$d_{eq}$	bubble equivalent diameter	$V_T$	terminal velocity
$e$	eccentricity	$x_c$	centroid abscissa
$EO$	Eötvös number, $EO = \frac{(\rho_l - \rho_g)gd_{eq}^2}{\sigma}$	$x_c^t$	displacement in $x$ direction
$f$	angular frequency	$y_c$	centroid ordinate
$F(x, y)$	gray value of output image	$y_c^t$	displacement in $y$ direction
$g$	acceleration of gravity	$z_c^t$	displacement in $z$ direction
$I(x, y)$	gray value of input image	$\Delta t$	time interval
$i$	abscissa of bubble pixel	$\mu$	dynamic viscosity
$j$	ordinate of bubble pixel	$\rho$	density
$L$	distance ascending in one revolution	$\sigma$	surface tension
$Mo$	Morton number, $Mo = \frac{g\mu_l^4}{(\rho_l - \rho_g)\sigma^3}$	$\omega$	angular velocity
$N$	total pixels	<b>Subscripts</b>	
$R$	camera rotation matrix	1	bubble shot at angle 1
$Re$	Reynolds number, $Re = \frac{\rho_l d_{eq} V_T}{\mu_l}$	2	bubble shot at angle 2
		$g$	gas
		$l$	liquid

## 1. INTRODUCTION

Bubble dynamics widely exist in many gas-liquid reaction devices, such as bubble column reactors, gas-liquid agitators, slurry reactors, separation devices and other gas-liquid contact devices (Lee and Lasa 1987; Pourtousi *et al.* 2015). Bubble movement is often accompanied by phase transitions, such as boiling, heat and mass transfer. Currently, many scholars employ numerical and experimental methods to study a single bubble rising behaviour in still water. Although this situation is relatively simple, it solves more common problems in actual industrial processes.

The heat and mass transfer efficiency of gas-liquid reactor is related to bubble motion characteristics. Bubble size is the most intuitive representation of gas-liquid motion process. The smaller the bubble is, the larger the gas-liquid relative area, which is conducive to the gas-liquid mass transfer process. However, when the bubble size changes, different rules can be elicited from the bubble rising trajectory (Naccache *et al.* 2019). Bubble trajectory is also one of the important factors affecting heat and mass transfer. Therefore, it is important to study the relationship between the bubble size and its trajectory for the design and operation of gas-liquid reactors. Saffman (1956) and Shew and Pinton (2006) used experimental and numerical simulation methods to study the bubble rising trajectory in still water, respectively. The critical diameters of straight and curved motion obtained by these two different methods are 1.4 mm and 1.94 mm respectively. Zhou *et al.* (2020) experimentally measured bubble rising trajectories with diameters of 0.32 mm-8.5 mm, and the results showed that 1 mm and 5.5 mm were the critical diameters for the bubble trajectories to be S-shaped and clutter-shaped in a two-dimensional (2D) plane, respectively. Shim *et al.* (2021) studied the instability of the bubble ascending path with diameters of 1 mm to 4 mm by numerical simulation. The simulation showed that when the bubble diameter was over 1.5 mm, the rising trajectory began to oscillate in a plane, and when the bubble diameter reached 4 mm, the oscillating plane began to distort. However, the curved motion of bubbles includes 2D zigzag and three-dimensional (3D) spiral motion, and the 2D method they used did not study the critical diameters of these two types of bubble motion.

In the process of studying the bubble rising trajectory in still water, Lewandowski *et al.* (2019) used the sine function to fit the bubble trajectory in the  $x$ -direction and found that the oscillation frequency of the bubble trajectory was closely related to the velocity of the liquid flow field, vortex shedding and induced turbulence kinetic energy. The bubble rising trajectory within the range of 2.2 mm-2.6 mm was fitted using sine function. However, more irregular trajectories of larger bubbles were not quantitatively discussed. Gong *et al.* (2022) experimentally measured the oscillation frequency of the rising trajectory of six sizes of bubbles with diameters ranging from 2.73 mm to 4.51 mm. Influenced by the inertial force and surface tension, the oscillation

frequency of the bubble trajectory decreases with the increasing bubble diameter. Although the frequency of the horizontal oscillations was successfully measured quantitatively, the 2D measurement ignored the bubble motion on another horizontal plane.

Furthermore, the bubble shape not only affects the flow behaviour of bubbles but also affects the heat and mass transfer efficiency of gas-liquid reaction devices. Li *et al.* (2019) and Mei and Cheng (2022) discussed bubble deformation with different diameters based on the volume of fluid (VOF) method. The former found that when bubble diameter was 3 mm, the bubble shape changed from oval to flat. When the bubble diameter was 5 mm, the bubble initial shape was spherical and then quickly changed into a flat circle. For bubbles with diameters of 7 mm and 9 mm, their shape changed irregularly due to severe deformation. The latter studied the resistance of bubbles with a diameter of 6 mm in the process of rising in still water. The resistance includes both pressure and viscous resistance. Since an increase in bubble size leads to an increase in viscous resistance and a decrease in pressure resistance to maintain balance, the bubble contour curved and presented a streamlined shape.

The bubble rising velocity is one of the important parameters to characterise bubble movement. An increase in bubble velocity enhances the turbulence in the gas-liquid reactor. Maldonado *et al.* (2013) experimentally measured bubble rising velocity with a diameter of 2.5 mm, and the results showed that the rising velocity was closely related to the bubble shape. When the force of a bubble reaches a quasi-equilibrium state, the resistance and buoyancy on the bubble is balanced. For a small bubble, the resistance and buoyancy are both small; for a large bubble, the large buoyancy corresponds to large resistance. Therefore, the relationship between the bubble terminal velocity and diameter is not monotonic. Nevertheless, their research lacked clear definitions and values for both small and large bubbles. Khorasanizadeh *et al.* (2021) used simulation and experimental methods to discuss the bubble terminal velocity in a bubble diameter range of 2.6 mm-3.5 mm. When the bubble diameter increases from 2.6 mm to 3.5 mm, the speed of the increase in resistance is greater than that of the increase in buoyancy; therefore, the large bubble will reach the terminal velocity faster than the small bubble, and the terminal velocity decreases with the increase in the bubble diameter within this range. However, this bubble diameter range is too small to successfully obtain the diameter when the increasing speed of resistance is equal to the increasing speed of buoyancy, that is, the minimum terminal velocity and its corresponding bubble diameter.

Although many scholarly works studied bubble rising behaviour in still water in the past, the bubble size, shape, trajectory and terminal velocity do not uniquely affect the heat and mass transfer efficiency of gas-liquid reaction devices but are instead coupled with each other; therefore, a single study on these parameters cannot reach a comprehensive conclusion regarding their effect on the heat and mass transfer

efficiency of gas-liquid reaction devices. In this study, the above bubble dynamic parameters are comprehensively analysed, and a systematic conclusion is obtained about their relationship.

Due to the limitations of experimental conditions and measurement methods, most previous studies on bubble rising behaviour provide 2D results; however, bubble rising behaviour is a complex and 3D process for which the dynamic characteristics cannot be fully reflected by 2D measurements. In the present study, the bubble behaviour is measured by a high-speed camera and virtual stereo vision technology. In Section 2, the experimental apparatus is explained, and the principle of 3D measurement is introduced; the results of camera calibration are given. In Section 3, the image processing and bubble parameter extraction methods are described. The ellipsoidal volume method uses the information from two perspectives to calculate the bubble equivalent diameter. In Section 4, the 3D measurement results of bubble shape, trajectory, displacement angular frequency and terminal velocity are discussed. In Section 5, the experimental results and theoretical conclusions are summarized.

## 2. EXPERIMENTAL SETUP AND PRINCIPLE

### 2.1 Experimental Setup

The experimental system is shown in Fig. 1. Figure 1(a) is the schematic diagram, and Fig. 1(b) is the actual photograph. The system consists of the injection pump, solenoid valve, rubber plug, water tank, needle, LED light source and high-speed camera. The injection pump is a muffle TSD 01-01-CE bidirectional push-pull type. Fast switching is achieved by a synchroniser that switches the positive and negative stroke of the syringe. Under the action of the injection pump, air is delivered to the needle where bubbles are generated. By controlling the speed of the syringe pump, there is only a single bubble in the shooting area. The injection rate is set at 4 ml/min. Needles with six different diameters are adopted, including 1.26 mm, 1.6 mm, 2.08 mm, 2.4 mm, 2.95 mm and 4 mm. The length of the needles is 60 mm. The rubber plug is used to fix the replaceable needle to produce bubbles with an equivalent diameter of 2.61 mm-5.11 mm. Ten sets of repeatability experiments are performed on each needle. The experiment repeatability errors and the bubble equivalent diameter standard deviations are shown in Fig. 2. The repeatability error increases with the increase in the needle diameter. The repeatability error range is 2.46% to 4.68%, and the maximum repeatability error occurs when the needle diameter is 4 mm. The bubble equivalent diameter is determined according to the average value of the entire bubble rise process. With the increase in the needle diameter, the bubble size also increases, which leads to serious bubble deformation, and the randomness of bubble sizes also increases. Bubble deformation will cause the standard deviation of the equivalent diameter to increase, and the maximum standard deviation is 0.0719 mm, which occurs when the bubble equivalent diameter is 5.11 mm. The

experimental section is a 150 mm×150 mm×500 mm water tank consisting of transparent acrylic plates, which are 4 mm thick. The lighting system used for the test is a parallel LED white light source with dimensions of 160 mm×160 mm, with light on the back. The shooting centre of this experiment is 200 mm from the bottom of the water tank. The shaded region in Fig. 1(a) is the measurement area, which is 70 mm×120 mm. Image acquisition is performed with a high-speed camera (Photron FASTCAM SA-Z). Images are recorded at 500 fps with an image resolution of 1024 × 1024 pixels.

### 2.2 Principle and Calibration

The virtual stereo vision is provided by a high-speed camera with a stereo imaging adapter, which facilitates forming two image views on the same

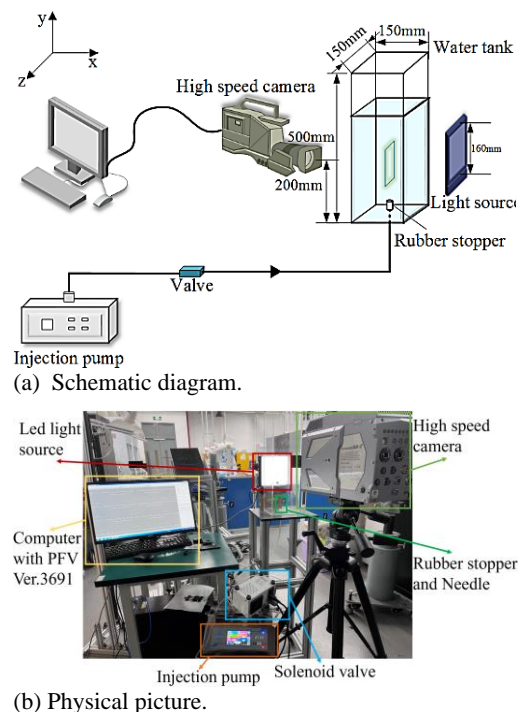


Fig. 1. Experimental apparatus.

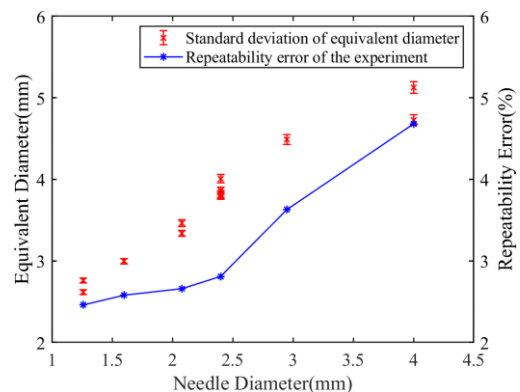
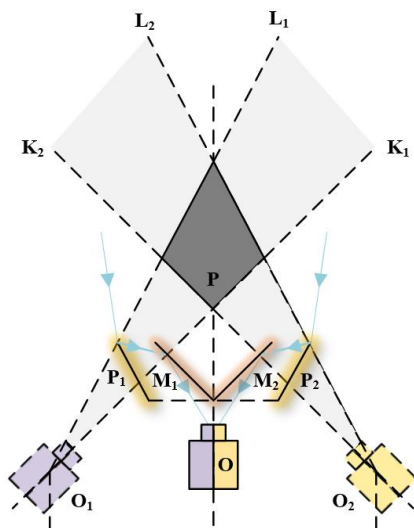
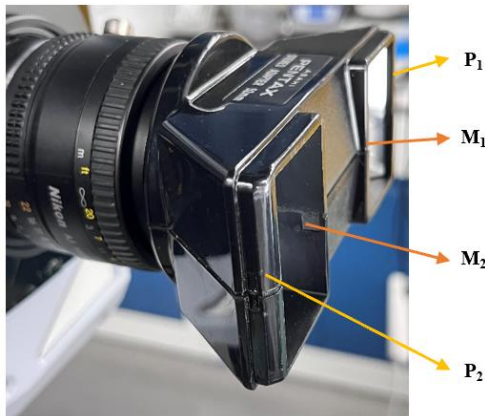


Fig. 2. Standard deviation and repeatability error.

imaging plane. The principle of 3D measurement by virtual stereo vision is shown in Fig. 3(a), and the actual virtual stereo vision image is shown in Fig. 3(b). The symmetrical mirror groups in the middle and on both sides are denoted as  $M_1$  and  $M_2$  and  $P_1$  and  $P_2$ , respectively.  $L_1$  and  $K_1$  represent the edge light along the virtual camera  $O_1$ , while  $L_2$  and  $K_2$  represent the edge light along the other virtual camera  $O_2$ . The overlap area of the two virtual cameras is shown as a deep shadow, forming a common observation section of the stereo system. The lights  $K_1$  and  $K_2$  intersect at point  $P$  on the optical axis of the real camera, which represents the nearest observable point along the optical axis. Through the refraction and prism path, a real camera can be mirrored into two symmetrical virtual images with intersecting optical axes. The image plane of a real camera is divided into left and right imaginary planes. When the bubble is observed, the measured characteristics are imaged in the field of view of two virtual cameras, thus forming a virtual stereoscopic parallax. The virtual stereoscopic vision does not require two precisely synchronised image signals, which effectively reduces the complexity and is relatively fast (Zhang *et al.* 2019).



(a) Principle of virtual stereo vision.



(b) Actual virtual stereo vision image.

**Fig. 3. Virtual stereo vision technology.**

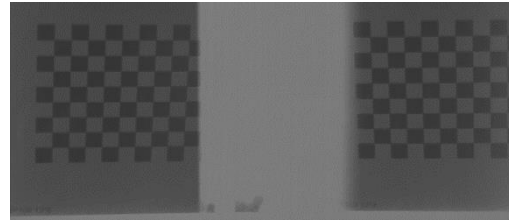


**Fig. 4. Underwater calibration plate image.**

Virtual stereo vision calibration is the foundation and precondition for 3D reconstruction. The calibration model is determined by the spatial attitude between two virtual cameras (rotation matrix  $R$  and shift vector  $T$ ), based on the principle of ray intersection orientation, with the help of characteristic points on the calibration board. The MATLAB toolbox *Stereo Camera Calibrator* is used for the calibration, which follows the strategy established by Zhang (2000). Figure 4 shows an image of a calibration board placed in the water tank, captured by the virtual stereo system. The small square size of this calibration board is 6 mm×6 mm.

The  $R$  and  $T$  matrices obtained in this study are as follows:

$$R = \begin{bmatrix} 0.8163 & 0.0160 & -0.5773 \\ -0.0368 & 0.9990 & -0.0243 \\ 0.5764 & 0.0411 & 0.8161 \end{bmatrix}$$

$$T = [-90.2988 \quad 2.0895 \quad 17.0015]^T$$

Factors such as the camera focal length, the angle of the optical axis and baseline, the camera distortion, and the placement of the calibration board will affect the calibration accuracy. The back-projection is calculated using the corner coordinates on two view images according to the obtained internal and external parameters. The ten sets of calibration images taken at different angles are evaluated by Eq. (1), while the results are shown in Fig. 5.

$$error = \frac{\sum_{i=1}^N \sqrt{(U_i - u_i)^2 + (V_i - v_i)^2}}{M} \quad (1)$$

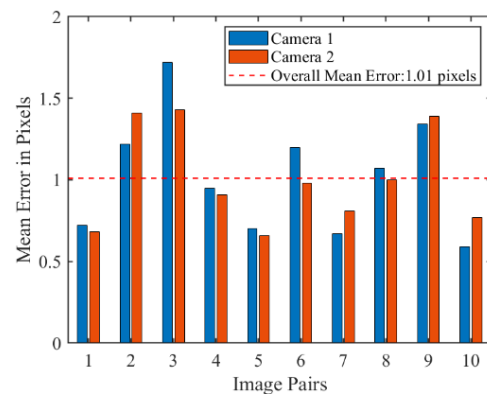


**Fig. 5. Illustration of the calibration error.**

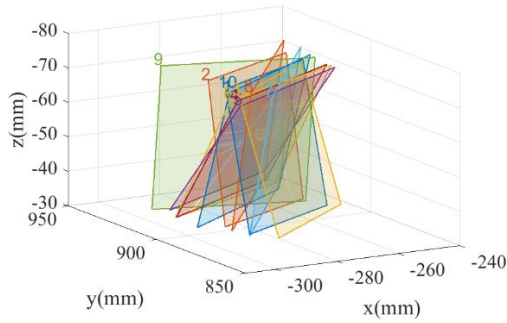


**Fig. 6. Illustration of the reconstruction error.**

In Eq. (1),  $M$  is the number of corners on all images.  $U_i$  and  $V_i$  are the actual image icons of the corners, and  $u_i$  and  $v_i$  are the calculated image coordinates. The overall mean error is 1.01 pixels in the current experimental setup.

The reconstruction results of the calibration board at ten different positions are shown in Fig. 6. The reconstructed 3D view of the ten planes shows little distortion, which demonstrates the accuracy of the calibration parameters and the 3D reconstruction algorithm. According to the obtained 3D coordinates of the calibration plate, the side length of the square can be calculated. The results indicate that the average error is less than 4% of the square side length.

### 3. IMAGE PREPROCESSING AND PARAMETER EXTRACTION

Due to the limitations of the experimental environment and equipment, there will inevitably be some interference during the experiment. The bubble image may exhibit problems, such as an uneven background, unclear contrast between the bubble and background, uneven bubble brightness, blurred bubble edges, etc. Therefore, before using the captured image to extract the bubble characteristic parameters, it is necessary to use an appropriate digital image processing algorithm for image preprocessing to improve the visual effect of the image, enhance the useful information of the image, and facilitate the extraction of characteristic parameters.

#### 3.1 Image Preprocessing

Figure 7 shows the digital image preprocessing procedure performed on the bubble images. The original image to be taken by the high-speed camera is shown in Fig. 7(a). First, the image is converted to the greyscale format, as shown in Fig. 7(b). Then, the image is binarised using the Otsu threshold method (Guo *et al.* 2014), with the value of 0 or 1 possible for each pixel. Assuming that  $I(x, y)$  is the grey value of the input image pixel,  $F(x, y)$  is the grey value of the output pixel, and the threshold is  $T_h$ , then:

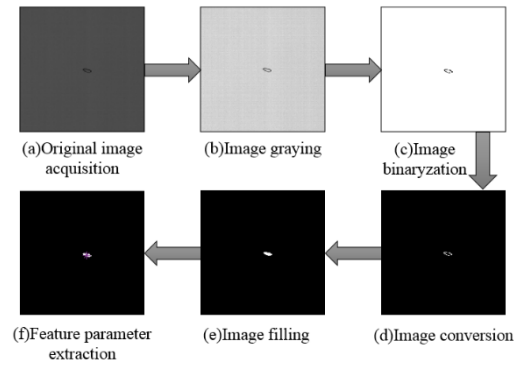


**Fig. 7. Bubble feature extraction process.**

$$F(x, y) = \begin{cases} 1, I(x, y) \geq T_h \\ 0, I(x, y) < T_h \end{cases} \quad (2)$$

Eq. (2) shows that the threshold has a great effect on the exact identification of the target area of the bubble during the digitisation of the image. If the selection threshold is too high, some bubble information will be lost. Conversely, when the threshold value is too small, part of the background will be mistaken for bubble information. Therefore, determining the best threshold is a key and difficult task for splitting the pertinent information. To ensure filling of subsequent bubbles and identification of characteristic parameters, the image is black/white inverted, as shown in Fig. 7(d). Then, the morphological closing operation is performed, after which the hole filling operation can be conducted. The filled image is shown in Fig. 7(e), which shows the closed area for the bubble region. After the image preprocessing, the characteristic parameters, such as centre, area and perimeter of the bubble, can be resolved.

#### 3.2 Extraction of Bubble Characteristic Parameters

In 2D measurement, the bubble diameter is regarded as a circle or an ellipse when calculating the bubble diameter. Bubble in the present study is regarded as an ellipsoid through 3D measurement, and the equivalent bubble diameter is calculated by the ellipsoidal volume method, which more closely represents situations encountered in reality. The maximum value in the two perspectives is the long axis of the ellipsoid, and the minimum value is the short axis. The axis length in the third direction is related to the eccentricity. When the eccentricity is small, the axis length in the third direction matches the length of the long axis; as the eccentricity increases, the value of the axis length and the short axis in the third direction is closer. Eq. (4) presents the relationship between the axial length in the third direction and the eccentricity. The bubble equivalent diameter  $d_{eq}$  is obtained from Eq. (6).

$$a = \max \{a_1, a_2\} \quad (3)$$

$$b = \min\{b_1, b_2\} \quad (4)$$

$$c = (a-b)e + b \quad (5)$$

$$d_{eq} = (abc)^{1/3} \quad (6)$$

In Eqs. (3-6),  $a$  is the ellipsoid major axis;  $b$  is the ellipsoid minor axis;  $c$  is the axis length of the ellipsoid in the third direction; and  $e$  is the eccentricity. The error in the determination of the bubble equivalent diameter is mainly due to the detection of bubble edges in digital image processing. According to results of [Bongiovanni \*et al.\* \(1997\)](#), the bubble equivalent diameter error estimates are reasonable in the range of  $\pm 1$  to  $\pm 2$  pixels.

The 2D geometric centroid of the bubble is the summation and average of the coordinates of all pixel points of the same bubble in the binarised filled image. The geometric centroid coordinate is calculated using Eq. (7).

$$\begin{cases} x_c = \sum \frac{i}{N} \\ y_c = \sum \frac{j}{N} \end{cases} \quad (7)$$

where  $i$  and  $j$  are the abscissa and ordinate of pixels of each pixel point in the bubble area, respectively.  $N$  is the total number of pixels in bubble area.  $x_c$  and  $y_c$  are the abscissa and ordinate of bubble centroid, respectively.

In the gas-liquid two-phase flow, the bubble velocity is a very important characteristic parameter. Eq. (8) can be obtained from the definition of velocity.

$$v' = \sqrt{\left(\frac{x_c^{t+\Delta t} - x_c^t}{\Delta t}\right)^2 + \left(\frac{y_c^{t+\Delta t} - y_c^t}{\Delta t}\right)^2 + \left(\frac{z_c^{t+\Delta t} - z_c^t}{\Delta t}\right)^2} \quad (8)$$

In Eq. (8),  $x_c^t$ ,  $y_c^t$  and  $z_c^t$  represent the displacement of the bubble in  $x$ -,  $y$ -,  $z$ -directions, respectively.  $v'$  is the instantaneous velocity magnitude of bubble movement, while  $\Delta t$  is the time interval between two adjacent pictures.

## 4. RESULTS AND DISCUSSION

### 4.1 Bubble Shape

The bubble images shown in Fig. 8(a)-(l) contain a typical bubble profile in the rising phase of the bubble, with a time interval at 0.02 s. The coordinate represents the distance from the needle exit. The findings show that when the bubble equivalent diameter is between 2.61 mm to 4.49 mm, the bubble shape is spherical or ellipsoid, while the shape is relatively stable during the rising process. When  $d_{eq}$  increases to 4.49 mm-5.11 mm, the shape of the bubble becomes irregular, resembling a crown.

During the bubble rising in still water, its shape changes from an ellipsoid (I) to a mushroom shape (II), and then to a hat shape (III). As the bubble rises, stable ellipsoidal bubbles were formed, as shown in Fig. 8(j)-(l). In this study, the bubbles were divided into two categories: large bubbles ( $d_{eq} \geq 4.49$  mm) and small bubbles ( $d_{eq} < 4.49$  mm), mainly depending on the shape deformation.

After the bubbles separate from the needles, they begin to rise under the action of buoyancy. The pressure at the top of the bubble is higher than the pressure at the bottom. The pressure difference and the vortex that develops on the bubble surface together induce a jet that pushes the bubble from below. [Magnaudet and Eames \(2000\)](#) concluded that the larger the bubble is, the greater the pressure difference induced by the top and bottom bubble surfaces, and the larger the jet generated at the bottom. The bottom jet has little effect on the bubble upper surface so that the velocity of the upper surface of the bubble is normally smaller than that of the rest. For large bubbles, the pressure difference between the upper and lower bubble surfaces is large, resulting in a large jet and velocity difference. Thus, the bubble will become flattened and receive greater resistance. Under the combined effects of buoyancy and hydrostatic resistance, the top and bottom of the bubbles are squeezed, showing obvious deformation. Moreover, as the diameter of the bubble increases, both the surface tension and its induced additional pressure inside the bubble decrease, so the bubble becomes more deformed. As the bubble rises, the influence of the jet on the bubble is reduced and stable ellipsoid bubbles are finally formed. In contrast, the pressure difference between the upper and lower surfaces of relatively small bubbles is not obvious. Therefore, the degree of bubble deformation is small and a spherical or ellipsoidal shape is maintained.

### 4.2 Three-dimensional Bubble Trajectory and Velocity

According to the calibrated intrinsic parameters of the camera and the rotation matrix  $R$  and translation vector  $T$  between the virtual cameras, 3D reconstruction is performed to obtain the space coordinates of the bubble centroid. Figure 8 shows the reconstructed 3D trajectories of bubbles with equivalent diameters ranging from 2.61 mm to 5.11 mm. The bubble rising trajectory is mainly determined by three aspects, namely, the mass force affected by the turbulence of the flow field, the wake instability caused by the vortex shedding from the bubble surface, and the shape change ([Mougin and Magnaudet 2001](#)). Additionally, since the resistance in all directions is no longer symmetrical due to bubble deformation during the rising process, the bubble will rise in the direction with the smallest resistance force. The pressure field generated by the asymmetric vortex shedding will also affect the rising trajectory.

For bubbles with spiral and zigzag trajectories, the trajectories obtained by 2D measurement methods

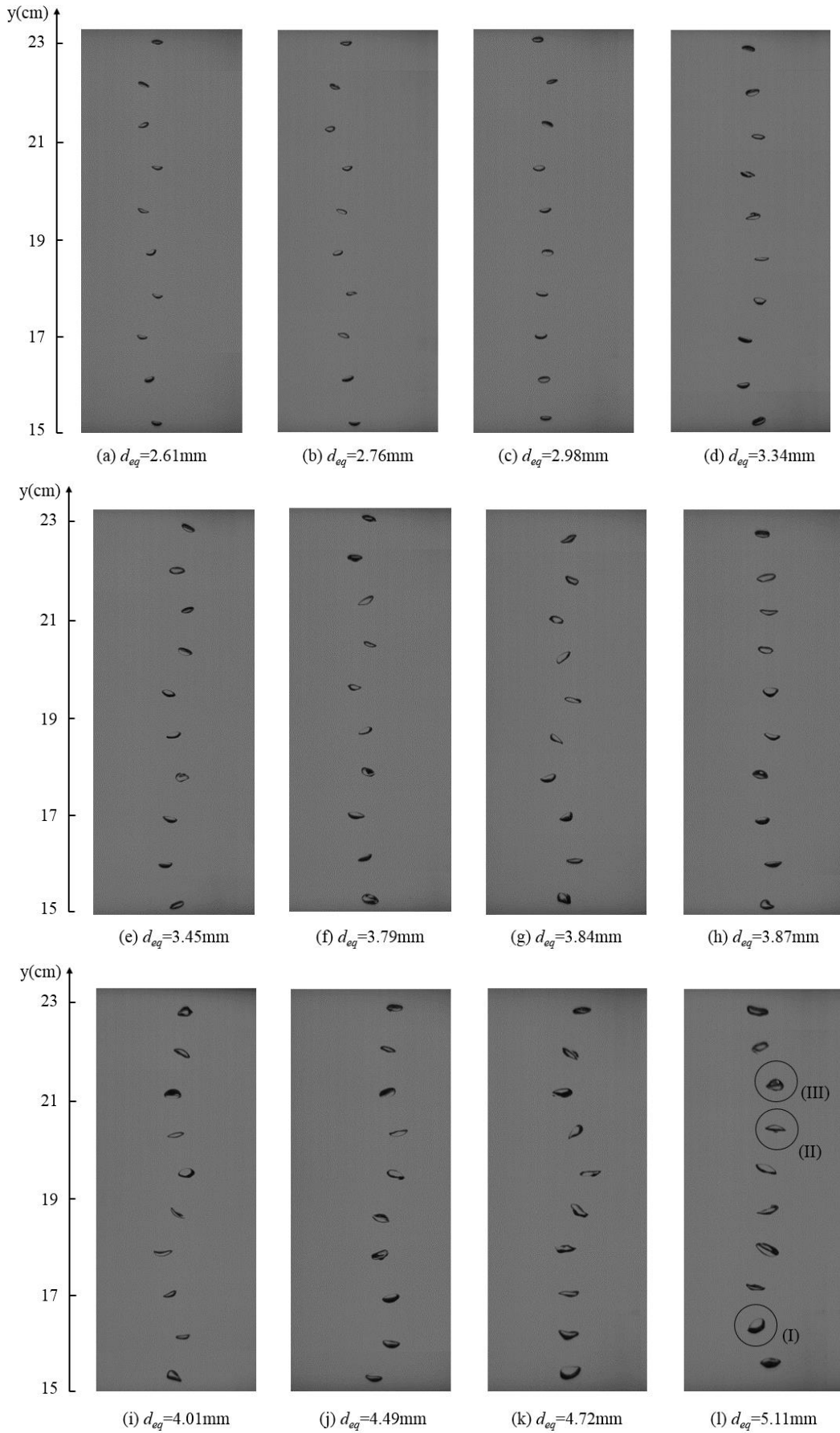


**Fig. 8. Images of bubbles with different equivalent diameters.**

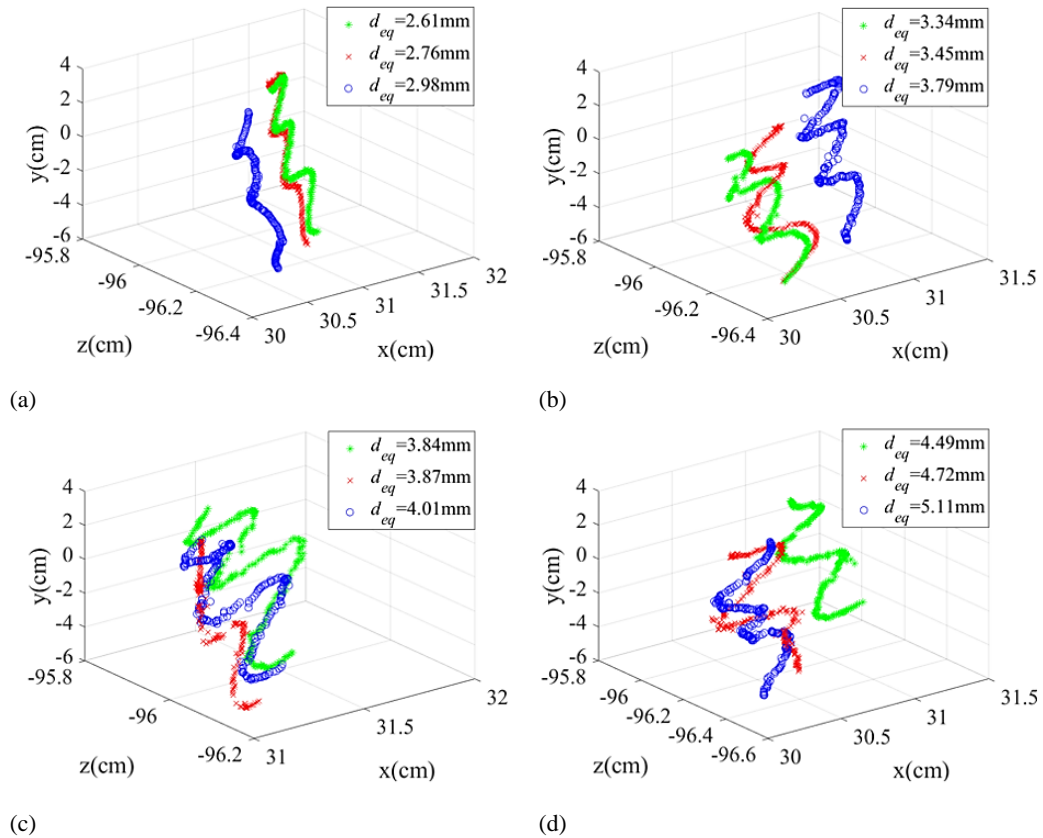


**Fig. 9. Three-dimensional trajectories of bubbles.**

are both S-shaped, and the difference between the two trajectories cannot be recognised. In contrast, 3D reconstruction of the bubble trajectory is conducted through 3D measurement to obtain the 3D visualisation of zigzag and spiral trajectories. As shown in Fig. 9(a)-(c), when the equivalent diameters of bubbles range from 2.61 mm to 4.01 mm, the rising trajectories spiral in 3D space. As shown in Fig. 8(a)-(i), when the bubbles are small, the shapes are deformed very little and almost remain spherical or ellipsoid. Therefore, the force change of the bubbles in the water is small, and the 3D trajectories are relatively stable. Due to the complex interactions between the gas phase and the liquid phase in the two-phase flow, there are uncertain factors during the ascent. The 3D trajectories of bubbles are not standard spirals, so the trajectory equation cannot be accurately expressed. The following uses the shape parameters  $L$  to roughly characterise the trajectories of bubbles with different equivalent diameters.  $L$  represents the distance that the trajectory rises in the  $y$ -direction during one revolution. The schematic diagram of  $L$  is shown in Fig. 10(a). When the bubble equivalent diameter changes,  $L$  changes with the bubble equivalent diameter, as shown in Fig. 10(b). Therefore,  $L$  increases with the increase in the bubble equivalent diameter. The increasing trend becomes more dramatic when the bubble equivalent diameter is between 3.45 mm and 4.01 mm.

As shown in Fig. 9(d), the trajectories with equivalent diameters of 4.49 mm-5.11 mm show S-

shaped movement after the initial release, and the trajectories are zigzag. Zigzag trajectories are unstable and irregular compared to spiral trajectories. In this case, Fig. 8(j)-(l) shows that the bubbles are quite large and the deformation must be considered. As the bubble deformation increases, the curvature of the bubble surface increases directly, and the vortex generated on the bubble surface becomes unstable. The wake instability is the direct cause of the unstable rising trajectory. Another reason is that the paired shedding of the bubble tail vortex proposed by Lunde (1997) will force the movement direction to deviate from the centre line of the release point, causing irregular changes in the rising trajectory.

The time interval between two adjacent frames of images is 0.002 s, so the 3D velocity of bubbles can be easily resolved based on the 3D trajectories. Figure 10 shows the velocity vectors  $u$ ,  $v$  and  $w$  with bubble equivalent diameters of 2.76 mm, 3.87 mm, 4.49 mm and 5.11 mm in three directions of  $x$ ,  $y$ ,  $z$ . During the rising process, the velocity vectors along the  $y$ -axis remain positive. When the bubble equivalent diameter is small (Fig. 11(a)), the bubble quickly reaches a stable  $v$  under the action of viscous force and surface tension. When the bubble equivalent diameter increases to 3.87 mm (Fig. 11(b)), the effect of buoyancy on the bubble increases, which leads to  $v$  first increasing and then reaching a relatively stable value. When the size of the bubble further increases (Fig.11(c)-(d)), the bubble is greatly affected by the inertial force, which

causes  $v$  to rapidly decrease to a stable value from a relatively high velocity at the first recorded frames. In contrast to the variation trend of  $v$ , the velocity vectors in the  $x$ - and  $z$ -directions show periodic oscillations, which correspond to the observed spiral or zigzag trajectories. The findings show that the velocity vector  $u$  exhibits sinusoidal-like fluctuations in all cases, while the amplitude is mainly between 10 m/s and -10 m/s. The velocity change in the  $z$ -

direction can be obtained by 3D measurement, which can clearly determine the critical diameter of the bubble spiral and zigzag trajectories. When the bubble rises in a spiral,  $u$  and  $w$  exhibit a sinusoidal-like motion in phase, while the amplitude of  $w$  is smaller than that of  $u$ . However, as shown in Fig. 11(c)-(d),  $w$  of the bubble in the zigzag trajectory oscillates slightly around zero.

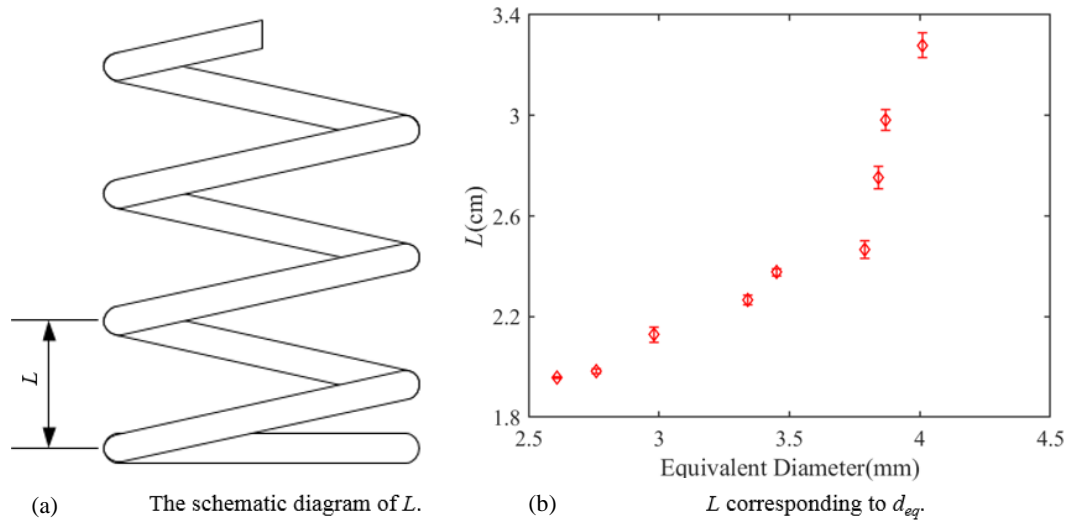


Fig. 10. Relationship between  $L$  and  $d_{eq}$  of spiral rising bubbles.

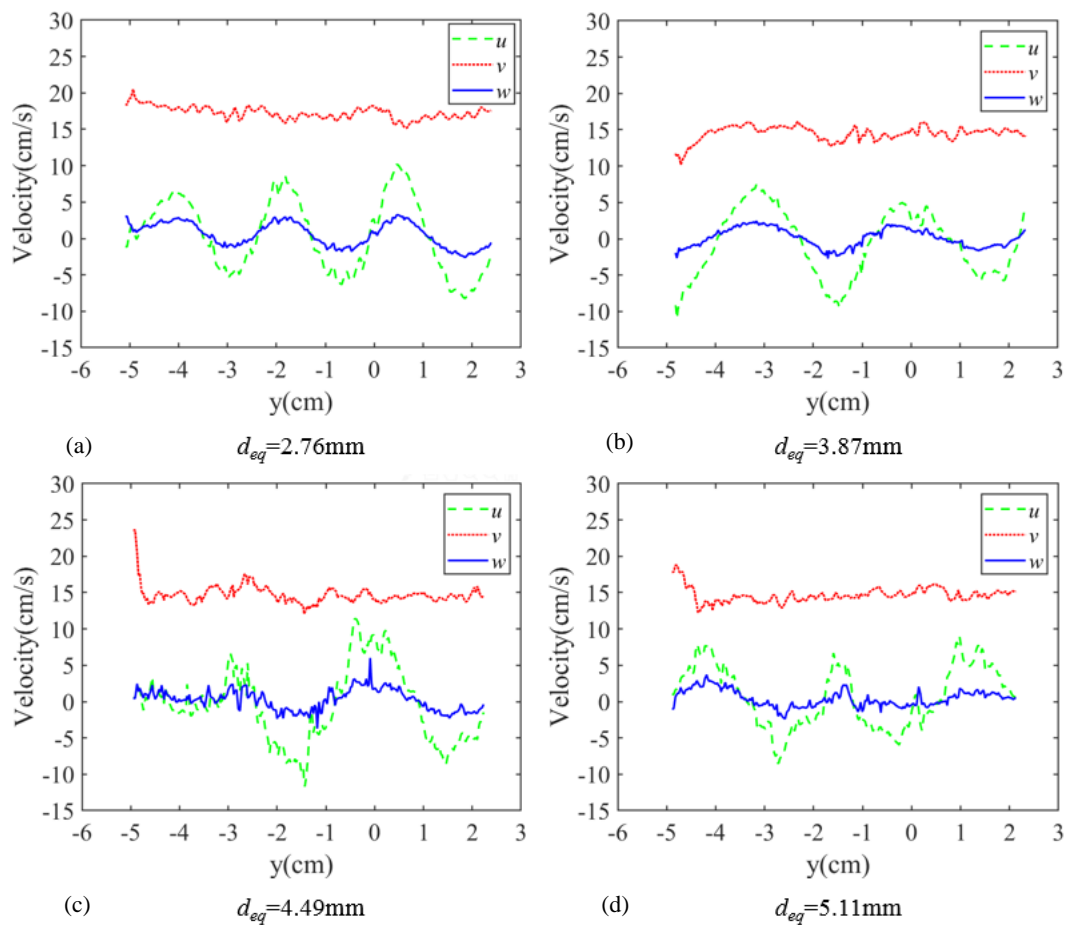
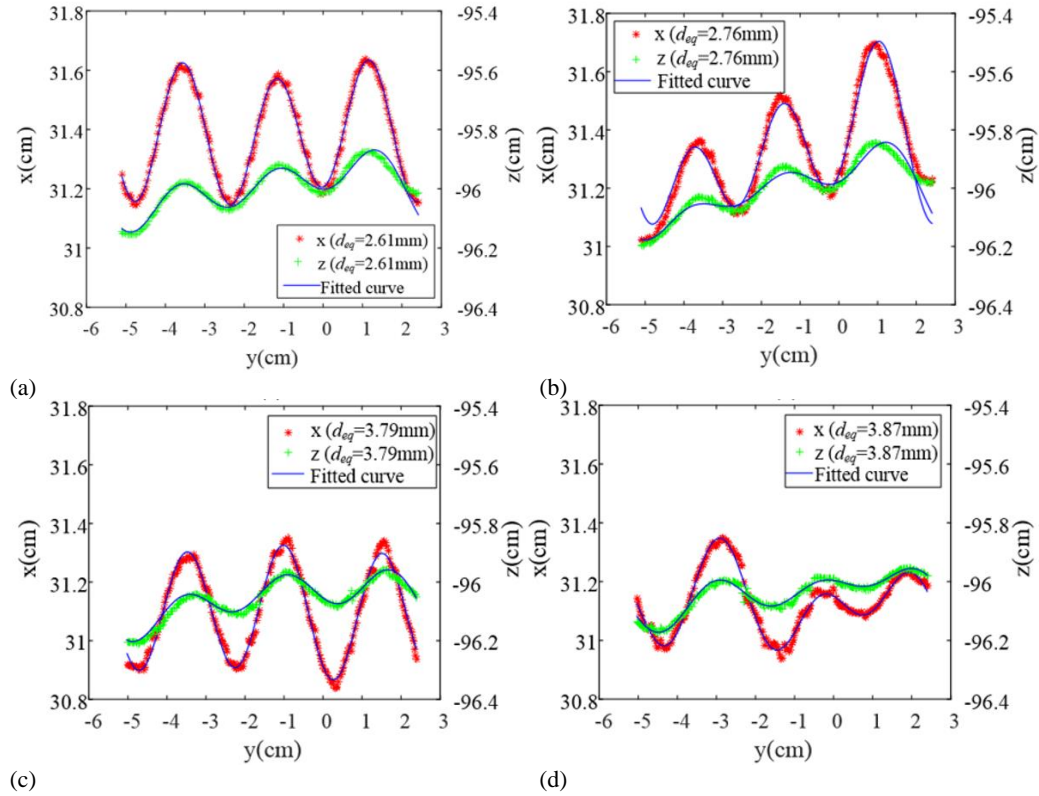


Fig. 11. Velocity variation of spiral and zigzag trajectories.



**Fig. 12. Bubble displacement with height in  $x$ - and  $z$ -directions.**

### 4.3 Displacement Angular Frequency

The 3D measurement results provide complete data for quantitatively describing the bubble displacement frequency oscillation on the horizontal plane. The bubble displacement with a spiral trajectory in  $x$ - and  $z$ -directions with the height  $y$  is plotted in Fig. 12. Ellingsen and Risso (2001) showed that the movement in the  $x$ -direction will produce a slow horizontal drift, causing the trajectory axis to tilt slightly, while the movement in the  $z$ -direction will cause the bubble to rotate slowly. Accordingly, the oscillation amplitude increases in the  $x$ -direction and decreases in the  $z$ -direction. For bubbles whose trajectories are spiral, there are no obvious phase differences in  $x$ - and  $z$ -directions. The bubble lift force is composed of two components, one of which makes the bubble move laterally, and the other makes the bubble stay on the vertical path. The movement of the bubble in the  $y$ -direction is the main mode. The movement in  $x$ - and  $z$ -directions is the secondary mode and appears as harmonic motion. Therefore, the experimental results are fitted with a third-order Fourier series, and the fitting accuracy is more than 95%. The displacement curves in  $x$ - and  $z$ -directions are expressed by Eqs. (9-10), respectively. The frequency of the displacement is shown in Table 1, while the value of the coefficients appearing in Eqs. (9-10) are shown in Tables 2-3.

$$x(y) = a_0 + a_1 \cos(w_x y) + b_1 \sin(w_x y) + \dots + a_3 \cos(3w_x y) + b_3 \sin(3w_x y) \quad (9)$$

$$z(y) = c_0 + c_1 \cos(w_z y) + d_1 \sin(w_z y) + \dots + c_3 \cos(3w_z y) + d_3 \sin(3w_z y) \quad (10)$$

In Eqs. (9-10),  $\omega_x$  and  $\omega_z$  are the bubble displacement angular velocity in the  $x$ - and  $z$ -directions, respectively.

As shown in Table 1, the angular frequency of bubble displacement in  $z$ -direction movement is 0.59 Hz-0.77 Hz smaller than that in the  $x$ -direction. As the bubble equivalent diameter increases from 2.61 mm to 3.87 mm, the bubble displacement angular frequency in both  $x$ - and  $z$ -directions gradually decreases. The  $f_x$  is reduced from 8.0262 Hz to 7.5567 Hz, and  $f_z$  is reduced from 7.3545 Hz to 6.9694 Hz. Gaudlitz and Adams (2009) proved by simulation that the frequency of bubble trajectory oscillation is consistent with the frequency of bubble wake shedding. Wang *et al.* (2018) pointed out that the bubble shedding frequency wake is proportional to the bubble rising velocity and inversely proportional to the equivalent diameter.

$$Sr = \frac{fd_{eq}}{V_T} \quad (11)$$

The Strouhal number is related to the Reynolds number, and its specific value can be found in Ern *et al.* (2012). The displacement frequency is calculated by Eq. (11), and the calculation results are listed in Table 1. The value of the calculated displacement angular frequency  $f$  is between the frequency  $f_x$  in the  $x$ -direction and the frequency  $f_z$  in  $z$ -direction.

**Table 1 Frequency of the bubble displacement in x- and z-directions**

Equivalent diameter	$f_x/(Hz)$	$f_z/(Hz)$	$f$ calculated by Eq. (11)
$d_{eq}=2.61$ mm	8.0262	7.3545	8.0077
$d_{eq}=2.76$ mm	7.8696	7.0963	7.4529
$d_{eq}=3.79$ mm	7.6845	6.9851	7.4190
$d_{eq}=3.87$ mm	7.5567	6.9694	7.1734

**Table 2 Coefficient of displacement fitting curve in x direction**

Equivalent diameter	$a_0$	$a_1$	$a_2$	$a_3$	$b_1$	$b_2$	$b_3$
$d_{eq}=2.61$ mm	31.39	0.01022	0.02564	-0.2199	0.02061	0.01504	0.0001047
$d_{eq}=2.76$ mm	31.33	0.1212	-0.036	-0.166	0.03459	0.08528	0.07058
$d_{eq}=3.79$ mm	31.1	-0.006998	-0.01169	-0.1683	-0.01258	-0.01109	-0.1233
$d_{eq}=3.87$ mm	31.13	-0.03042	-0.006754	0.05779	0.002992	0.09061	-0.09142

**Table 3 Coefficient of displacement fitting curve in z direction**

Equivalent diameter	$c_0$	$c_1$	$c_2$	$c_3$	$d_1$	$d_2$	$d_3$
$d_{eq}=2.61$ mm	-96	0.06412	-0.005128	-0.0606	0.002057	0.03902	-0.02918
$d_{eq}=2.76$ mm	-96.01	0.1028	-0.0199	-0.05174	0.004111	0.0539	-0.009701
$d_{eq}=3.79$ mm	-96.06	0.05807	-0.02161	-0.03021	-0.005032	0.0236	-0.05652
$d_{eq}=3.87$ mm	-96.04	0.04459	-0.03186	0.03135	0.01574	0.03509	-0.03669

Therefore, it can be concluded that the experimental results are in good agreement with the calculated results. The main mode of bubble motion is determined, while the motion of the secondary mode is related to the conditions of the experiment. The combination of the primary mode motion of the bubble in the y-direction and the secondary mode motion in x- and z-directions results in a complex trajectory. Therefore, without a complete 3D measurement, the characteristics of bubble movement can hardly be determined.

#### 4.4 Terminal Velocity

When the bubble reaches a steady state, the terminal velocity oscillates slightly. The bubble terminal velocity in 2D measurement is only the resultant velocity in two directions, while 3D measurement yields the resultant velocity in three directions, which effectively improves the accuracy of bubble terminal velocity measurement. In the current study, the terminal velocity is taken as the average value of the rising velocity when the bubble is 18 cm-22 cm away from needle exit. The standard error caused by the average value of the bubble terminal velocity is calculated by Eq. (12), which is 4% in the current experimental setup. The bubble terminal velocity in

2D measurement is only the resultant velocity in two directions, while 3D measurement yields the resultant velocity in three directions, which effectively improves the accuracy of bubble terminal velocity measurement. When  $2.61 \text{ mm} < d_{eq} < 5.11 \text{ mm}$ , the main factor affecting the bubble rising velocity is the friction between the two-phase interface. As the bubble equivalent diameter increases, the contact area between bubble and water increases, the frictional force increases and the bubble rising velocity decreases. In contrast, when bubble equivalent diameter is greater than 4.49 mm, the main influencing factor becomes buoyancy. As the bubble equivalent diameter increases, the buoyancy increases, and the rising velocity of the bubble increases. The minimum value appears for  $d_{eq}=4.49 \text{ mm}$  at 16.17 cm/s.

$$Std = \sqrt{\frac{(V_1 - V_T)^2 + (V_2 - V_T)^2 + \dots + (V_n - V_T)^2}{n - 1}} \quad (12)$$

The equivalent diameters of the bubbles in this experiment ranged from 2.61 mm to 5.11 mm, while the values of each dimensionless parameter of the bubble are:  $0.91 < Eo < 3.50$ ,  $492 < Re < 844$ ,  $Mo = 1.69 \times 10^{-11}$ . Clift *et al.* (1978) proposed that the value of  $Eo$  is 0.25-4 when the bubble is in a state dominated by surface tension. The experimental

results indicated that in pure water, the bubble terminal velocity first decreases with the increase in the equivalent diameter. When  $d_{eq}=5$  mm, the terminal velocity decreases to a minimum value of 20 cm/s, and then it gradually increases. Liu *et al.* (2016) proposed that when  $0.83 \text{ mm} < d_{eq} < 6 \text{ mm}$ ,  $0.09 < Eo < 4.67$  and  $87.24 < Re < 1064$ , the bubble is in a state dominated by surface tension. Both criteria indicate that the bubbles investigated in the current study are in a state dominated by surface tension. Therefore, the relational expression proposed in this study is applicable to bubbles in the state dominated by surface tension. The curve of this experiment has a similar trend to the results in Clift *et al.* (1978), which first decreases and reaches the minimum value at 4.49 mm. The terminal velocity then slightly increases with the increase in the bubble diameter. The discussion of bubble shape in Section 4.1 shows that 4.49 mm is the critical equivalent diameter for large and small bubbles, which is also the critical size for the bubble to begin to deform. The discussion of the bubble trajectory in Section 4.2 indicates that when the bubble equivalent diameter exceeds 4.49 mm, the trajectory will change from a spiral to a zigzag. Therefore, the following conclusions can be drawn: when the bubble begins to deform, the bubble trajectory will become a zigzag, accompanying the minimum terminal velocity.

As shown in Table 2, many scholars have proposed models to predict the bubble terminal velocity. The results from this study are compared with the prediction models and experimental data from Tomiyama *et al.* (2002) for the bubble terminal velocity in still water, as shown in Fig. 13. Due to a variety of factors, such as the diameter of the needle that generates the bubble, the injection rate of the syringe pump, and the possible presence of impurities in the tap water, it is reasonable for the experimental results of the terminal velocity to differ from the predictive models or experimental results proposed by other scholars. The comparison indicates that the overall trend of the experimental data in Tomiyama *et al.* (2002) is in good agreement with the current results: both data sets indicate that

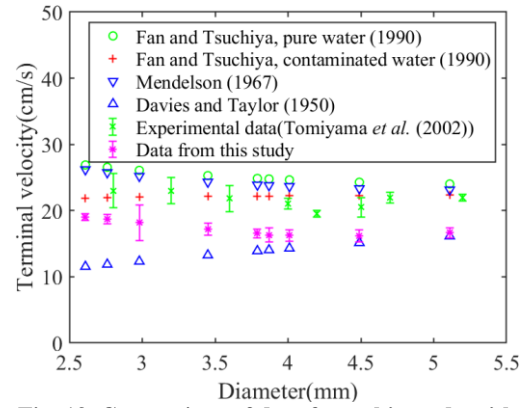


**Fig. 13. Comparison of data from this study with studies by other scholars.**

the bubble terminal velocity reaches a minimum value when the bubble equivalent diameter is approximately 4.5 mm. Notably, when  $d_{eq} < 4.49$  mm, although the models of Fan and Tsuchiya (1990) (pure water) and Mendelson (1967) overestimate the bubble terminal velocity, they perform well in terms of correlation. This shows that the models of Fan and Tsuchiya (pure water) (1990) and Mendelson (1967) are more accurate in predicting the terminal velocity of small bubbles with or without small deformations. The variation trend of the terminal velocity prediction models of Fan and Tsuchiya (1990) (contaminated water) and Davies and Taylor (1950) have the same law when  $d_{eq} \geq 4.49$  mm, indicating that these models are better at predicting the terminal velocity after the bubble is deformed. Therefore, to achieve the best prediction accuracy, when the bubble shape remains spherical or ellipsoidal ( $d_{eq} < 4.49$  mm in this experiment), the prediction model proposed by Mendelson (1967) can be used to predict the bubble terminal velocity. The model of Davies and Taylor (1950) can be used to predict the bubble terminal velocity when there is obvious bubble deformation ( $d_{eq} \geq 4.49$  mm in this experiment).

**Table 2 Predictive models for the bubble terminal velocity**

Investigator	Correlations	Remarks
Fan and Tsuchiya (1990)	$V_T = (V_1^{-n} + V_2^{-n})^{-1/n}$ $V_1 = \frac{\rho_l g d_{eq}^2}{K_b \mu_l}$ $V_2 = \sqrt{\frac{2q\sigma}{d\rho_l} + \frac{gd_{eq}}{2}}$ $K_b = \max(12, K_{bo} Mo^{-0.038})$	$K_{bo} = 14.7$ (water) $K_{bo} = 10.2$ (organic mixtures) $n = 1.6$ (pure water) $n = 0.8$ (contaminated water) $q = 1.2$ (single liquid) $q = 1.4$ (multi-liquids)
Mendelson (1967)	$V_T = \sqrt{\frac{2\sigma}{d_{eq}(\rho_l + \rho_g)} + \frac{gd_{eq}}{2}}$	Bubbles dominated by surface tension and buoyancy
Davies and Taylor (1950)	$V_T = 1.02 \sqrt{\frac{gd_{eq}}{2}}$	Bubbles rise in various liquids

## 5. CONCLUSION

This paper uses high-speed imaging and virtual stereo vision technology to capture the rising process of bubbles in still water. The 3D motion characteristics of bubbles are obtained by image processing and 3D reconstruction. The efficiency of the heat transfer quality of a gas-liquid reaction device not only needs to consider the bubble size but also needs to evaluate other characteristic parameters, including the bubble shape, rising trajectory, displacement angular frequency and terminal velocity, which have a strong correlation with the bubble size. Therefore, these parameters need to be comprehensively analysed and discussed. A bubble is regarded as an ellipsoid in the 3D measurement rather than a circle or ellipse in the 2D method, and the equivalent diameter is calculated by the ellipsoidal volume method. To better describe the bubble behaviour, bubbles are divided into small bubbles ( $d_{eq} < 4.49$  mm) and large bubbles ( $d_{eq} \geq 4.49$  mm) according to the degree of bubble deformation. At the same time, 4.49 mm is also the critical equivalent diameter of spiral and zigzag bubble trajectories. The small bubbles are stable in shape during the ascent and remain spherical or ellipsoid, exhibiting spiral paths in 3D space. In contrast, the pressure difference between the upper and lower surfaces of large bubbles ( $d_{eq} \geq 4.49$  mm) becomes significant, resulting in the flattening of the bubble surface and larger resistance. Under the action of buoyancy and hydrostatic resistance, the bubbles are more deformed. Moreover, the increase in the bubble equivalent diameter reduces the surface tension and pressure inside, resulting in greater deformation of large bubbles. Various forms of the bubble shape can be observed, including ellipsoid, mushroom, and hat. Due to the asymmetric force generated by bubble deformation and the unstable wake vortex generated during the ascent, the trajectory of large bubbles is a zigzag. The displacement curve in the horizontal direction is fitted by the third-order Fourier function, and the fitting accuracy is more than 95%. The bubble displacement angular frequencies in  $x$ - and  $z$ -directions are obtained through functional expressions, and they are quantitatively analysed. Both of them decrease with the increase in the bubble equivalent diameter. Furthermore, in all test cases, the frequency in the  $x$ -direction is less than that in the  $z$ -direction. This conclusion provides experimental data support for some theoretical analysis.

When the bubble trajectory is a 3D spiral, the 3D velocity analysis indicates that the velocity vectors in the  $x$ - and  $z$ -directions show periodic oscillations with no obvious phase difference, while the former has a larger oscillating amplitude. The terminal velocity measured at the stable rising state shows an initial decreasing and then increasing trend with the increase in the equivalent diameter. This is mainly due to the force changes caused by the bubble size and deformation. The experimental results are in good agreement with previously reported tests. However, most theoretical models are still unable to predict changes in the entire test range. This study discusses the applicability of classic bubble terminal velocity prediction models proposed by several

scholars. Based on the data set of this experiment and a comparison with the prediction model proposed by each scholar, the application scope of different models can be obtained, and the best prediction model under different conditions can be selected. The 3D measurement results of this study not only provide theoretical support and guidance for the design and operation of gas-liquid reaction devices but also provide reliable experimental evidence for theoretical analysis and numerical simulation.

## ACKNOWLEDGEMENTS

This work is supported by the National Natural Science Foundation of China (Grant No.: 51976121). Support from the jointly funded project by The Royal Society and Natural Science Foundation of China International Exchanges Scheme (Grant Nos. 52011530187 and IEC\NSFC\191536), is also gratefully acknowledged.

## REFERENCES

- Bongiovanni, C., J. P. Chevaillier and J. Fabre (1997). Sizing of bubbles by incoherent imaging: defocus bias. *Experiments in Fluids* 23(3), 209-216.
- Clift, R., J. R. Grace and M. E. Weber (1978). *Bubbles, Drops, and Particles*. Academic Press.
- Davies, R. M. and G. I. Taylor (1950). The mechanics of large bubbles rising through extended liquids and through liquids in tubes. *Proceedings of the Royal Society of London. Series A. Mathematical and Physical Sciences* 200(1062), 375-390.
- Ellingsen, K. and F. Risso (2001). On the rise of an ellipsoidal bubble in water: oscillatory paths and liquid-induced velocity. *Journal of Fluid Mechanics* 440, 235-268.
- Ern, P., F. Risso, D. Fabre and J. Magnaudet (2012). Wake-induced oscillatory paths of bodies freely rising or falling in fluids. *Annual Review of Fluid Mechanics* 44, 97-121.
- Fan, L. S. and K. Tsuchiya (1990). Bubble wake dynamics in liquids and liquid-solid suspensions. *Butterworth-Heinemann* 71-110.
- Gaudlitz, D. and N. A. Adams (2009). Numerical investigation of rising bubble wake and shape variations. *Physics of Fluids* 21(12), 1-9.
- Gong, Z., J. Cai, B. Tan, F. Chen and R. Deng (2022). Vorticity dynamics using PIV: Quantitative analysis of water perturbation by bubble rise. *Progress in Nuclear Energy* 153, 104414.
- Guo, W. Y., X. F. Wang and X. Z. Xia (2014). Two-dimensional Otsu's thresholding segmentation method based on grid box filter. *Optik* 125(18), 5234-5240.
- Khorasanizadeh, N., M. Karamoozian and H. Nouri-Bidgoli (2021). An experimental and cfd

- investigation on effect of initial bubble diameter on its rise velocity profile in A laboratory-scale flotation column cell. *Journal of Mining and Environment* 12(4), 1089-1102.
- Lee, S. L. P. and H. I. Lasa (1987). Phase holdups in three-phase fluidized beds. *AIChE Journal* 33(8), 1359-1370.
- Lewandowski, B., M. Fertig, M. Ulbricht and G. Krekel (2019). Relationship between bubble characteristics and hydrodynamic parameters for single bubbles in presence of surface active agents. *Chemical Engineering Science* 199, 179-198.
- Li, X., P. Zhang, J. Li, W. Wang and G. Chen (2019). Analysis of deformation and internal flow patterns for rising single bubbles in different liquids. *Chinese Journal of Chemical Engineering* 27(4), 745-758.
- Liu, L., H. Yan, G. Zhao and J. Zhuang (2016). Experimental studies on the terminal velocity of air bubbles in water and glycerol aqueous solution. *Experimental Thermal and Fluid Science* 78, 254-265.
- Lunde, K. (1997). Observations on wakes behind spheroidal bubbles and particles. *ASME Fluids Engineering Division Summer Meeting*.
- Magnaudet, J. and I. Eames (2000). The motion of high-reynolds-number bubbles in inhomogeneous flows. *Annual Review of Fluid Mechanics* 32(1), 659-708.
- Maldonado, M., J. J. Quinn, C. O. Gomez and J. A. Finch (2013). An experimental study examining the relationship between bubble shape and rise velocity. *Chemical Engineering Science* 98, 7-11.
- Mei, Z. and X. Cheng (2022). Modeling of interfacial area for single deformed bubble based on VOF method. *Nuclear Engineering and Design* 395, 111864.
- Mendelson, H. D. (1967). The prediction of bubble terminal velocities from wave theory. *AIChE Journal* 13(2), 250-253.
- Mougin, G. and J. Magnaudet (2001). Path instability of a rising bubble. *Physical Review Letters* 88(1), 014502.
- Naccache, M. F., A. A. Abdu and C. Abreu (2019). Air bubbles displacement in yield stress fluids. *Journal of Applied Fluid Mechanics* 13(2), 727-736.
- Pourtousi, M., P. Ganesan, A. Kazemzadeh, S. C. Sandaran and J. N. Sahu (2015). Methane bubble formation and dynamics in a rectangular bubble column: A CFD study. *Chemometrics and Intelligent Laboratory Systems* 147, 111-120.
- Saffman, P. G. (1956). On the rise of small air bubbles in water. *Journal of Fluid Mechanics* 1(3), 249-275.
- Shew, W. L. and J. F. Pinton (2006). Dynamical model of bubble path instability. *Physical Review Letters* 97(14), 144508.
- Shim, G., J. Kim and C. Lee (2021). Path instability of a no-slip spheroidal bubble in isotropic turbulence. *Physical Review Fluids* 6(7), 073603.
- Tomiyama, A., G. P. Celata, S. Hosokawa and S. Yoshida (2002). Terminal velocity of single bubbles in surface tension force dominant regime. *International Journal of Multiphase Flow* 28(9), 1497-1519.
- Wang, S., L. Liu, S. B. Zhang, F. B. Wen and X. Zhou (2018). Stability analysis of the onset of vortex shedding for wakes behind flat plates. *Theoretical and Computational Fluid Dynamics* 32(4), 411-423.
- Zhang, T., Y. Qian, J. Yin, B. Zhang and D. Wang (2019). Experimental study on 3D bubble shape evolution in swirl flow. *Experimental Thermal and Fluid Science* 102, 368-375.
- Zhang, Z. (2000). A flexible new technique for camera calibration. *IEEE Transactions on Pattern Analysis and Machine Intelligence* 22(11), 1330-1334.
- Zhou, Y., P. Kang, Z. Huang, P. Yan, J. Sun, J. Wang and Y. Yang (2020). Experimental measurement and theoretical analysis on bubble dynamic behaviors in a gas-liquid bubble column. *Chemical Engineering Science* 211, 115295.